# Analysis and Experiment of 5-DOF Decoupled Spherical Vernier-Gimballing Magnetically Suspended Flywheel (VGMSFW)

QIANG LIU [ID]1, HENG LI [ID]1, WEI WANG [ID]1, CONG PENG [ID]2, (Member, IEEE), AND ZENGYUAN YIN [ID]3

1Institute of Precision Electromagnetic Equipment and Advanced Measurement Technology, Beijing Institute of Petrochemical Technology, Beijing 102617, China
2College of Automation Engineering, Nanjing University of Aeronautics and Astronautics, Nanjing 210016, China
3Department of Aerospace Science and Technology, Space Engineering University, Beijing 101416, China

Corresponding author: Wei Wang (shaowang66@163.com)

**ABSTRACT** Due to the capacity of outputting both the high precision torque and the instantaneous large torque, the vernier-gimballing magnetically suspended flywheel (VGMSFW) is regarded as the key actuator for spacecraft. In this paper, a 5-DOF active VGMSFW is presented. The 3-DOF translation and 2-DOF deflection motions of the rotor are respectively realized by the spherical magnetic resistance magnetic bearings and the Lorentz magnetic bearing. The mathematical model of the deflection torque is established, and the decoupling between the 2-DOF deflections is demonstrated by the numerical analysis method. Compared with the conventional cylindrical magnetic bearings-rotor system, the spherical system is proven to eliminate the coupling between the rotor translation and deflection. In addition, a set of spherical magnetic resistance magnetic bearings with six-channel decoupling magnetic circuit are adopted to achieve the 3-DOF translation decoupling. The rotor dynamic model is derived, and the control system is established. The decoupling experiments and the torque experiments of the prototype are carried out. The results show that the decoupling among 5-DOF motions is realized and the instantaneous large torque can be obtained, which indicates that the requirements of the spacecraft can be highly satisfied by the spherical VGMSFW.

**INDEX TERMS** VGMSFW, spherical magnetic resistance magnetic bearing, Lorentz magnetic bearing, 5-DOF decoupled.

## I. INTRODUCTION

The ball bearing flywheels and the control moment gyroscopes are usually used for three-axis attitude stability control of spacecraft [1]–[3]. Flywheels are suitable for high-precision attitude pointing and high-stability attitude control because of the high precision output torque [4], [5]. However, the rapid maneuvering requirement for the spacecraft is hard to meet. By means of control moment gyroscopes with the advantage of large output torque, it is easy to achieve the fast attitude maneuver for the large-scale spacecraft [6]–[8], but difficult to guarantee the control precision [9], [10]. The limitations above can be remedied when

The associate editor coordinating the review of this manuscript and approving it for publication was Halil Ersin Soken [ID].

the gimballing flywheels integrating advantages of the flywheels with high precision torque and the control moment gyroscopes with large torque is used [11], [12]. The attitude control precision of spacecraft with gimballing flywheel is insufficient on account of the mechanical friction and vibration of the ball bearing [13], [14]. Owing to the advantages of no stiction-friction effect, virtually zero wear, long service life, high control precision, micro vibration and so on [15], [16], the VGMSFWs [17]–[30] are the attractive inertial actuator for the remote sensing satellites and the space telescopes. Two working modes including high precision and agile maneuver can be used for the VGMSFWs. In the former mode, the high precision attitude control is realized by controlling the rotor rotating speed. In the latter mode, the instantaneous large control torque is generated by tilting

the high-speed rotor. Simultaneously, the rapid stability of the spacecraft attitude is realized when the rotor vibration is suppressed with the help of the magnetic suspension technique.

The magnetic bearing (MB) can be categorized as the magnetic resistance MB and the Lorentz MB. The former with the advantages of high rigidity and low power consumption are widely adopted in the early VGMSFWs. C. Murakami *et al.* [17] presented a 3-DOF VGMSFW with an axial magnetic resistance MB for three-axis control. The axial translation and radial deflections of the rotor are controlled by two pairs of independent coils, and the radial translation stability are passively realized by permanent magnets. Seddon and Pechev [18] proposed another axial passive suspension scheme of VGMSFW for 4-DOF attitude control. Its radial translations and deflections are realized by a radial magnetic resistance MB. In order to remedy the limitations of passive suspension schemes in [17], [18] with the low precision torque, Horiuchi *et al.* [19] adopted the electromagnetic magnetic resistance MBs to achieve 5-DOF active suspension of the flywheel rotor. The suspension consumption is high as the bias magnetic flux and the control magnetic flux are both generated by the coil currents. Wen and Fang [20] and J. Tang *et al.* [21] respectively proposed another VGMSFW with the permanent magnet biased magnetic resistance MBs. The bias magnetic flux of the electromagnetic magnetic resistance MBs in [19] is replaced by that of the permanent magnet. Based on it, Peng *et al.* [22] introduced a synchronous vibration control method with a two-stage notch filter to suppress the vibration of the rotor. To improve the inertia-mass ratio of the flywheel rotor, Xie *et al.* [23] proposed an outer rotor VGMSFW with conical configuration. The load-bearing MBs were used for simulating the space weightless environment during ground testing. Saito *et al.* [24] developed another similar VGMSFW, which was carried on the "SERVIS-2" satellite launched in 2010. The control precision in [17]–[24] are relatively low due to the poor linearity of the magnetic resistance MB, and the complexity of the control systems is increased.

The Lorentz MBs with good linearity and no displacement stiffness, are more suitable for the high-precision and stable suspension of the flywheel rotor. Gerlach *et al.* [25] introduced the scheme of the VGMSFW manufactured by the Rockwell Collins Deutschland GmbH (formerly Teldix). The radial/axial translations and deflections are all controlled by Lorentz MBs. Liu *et al.* [26] put forward another similar scheme, and the attitude control and the attitude sensitivity of VGMSFW were analyzed systematically. When the coil current is constant, the electromagnetic force generated by the Lorentz MB is less than that produced by the magnetic resistance MB.

Combining the magnetic resistance MBs with large bearing capacity and the Lorentz MBs with high control precision, Li *et al.* [27] presented a hybrid VGMSFW. Similar to the schemes in [17], [18], the control precision is limited on account of the passive axial suspension force. Xiang and Tang *et al.* [28], Tang *et al.* [29] proposed a conical hybrid
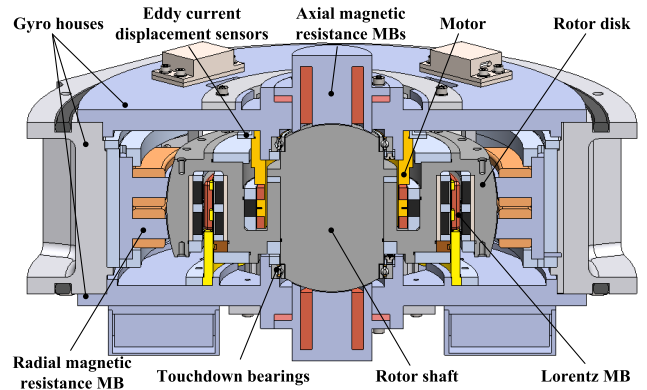


**FIGURE 1.** Schematic illustration of the spherical VGMSFW.

VGMSFW to achieve 5-DOF active control. The decoupling between the deflection force and the translation force is realized when the forces passes through the rotor centroid. Based on it, Liu *et al.* [30] introduced another hybrid VGMSFW with conical spherical hybrid magnetic resistance MBs.

In the schemes above, when the rotor is tilted, the interference torque is induced due to the change of the magnetic air gap with cylindrical shell, thin-wall and conical shell. To eliminate the coupling among 5-DOF motions, a novel spherical VGMSFW developed to meet the ever-increasing precision and maneuverability requirements of the spacecrafts is presented in this paper. The spherical magnetic resistance MBs-rotor system is adopted for decoupling between the rotor translation and deflection. The mathematical models of the rotor deflection and translation are established. The electromagnetic forces and the electromagnetic torques are analyzed. The decoupling experiment and torque experiment of the prototype are carried out.

## II. STRUCTURE AND PRINCIPLE OF THE SPHERICAL VGMSFW

As shown in Figure 1, the VGMSFW is mainly composed of a sphere rotor, three spherical magnetic resistance MBs, a Lorentz MB, a motor and twelve eddy current displacement sensors. The sphere rotor driven by the brushless DC motor is utilized to output the gyroscopic moment by changing the rotor speed and the rotating shaft of the rotor at high speed. The stable suspension and the translational control in radial and axial directions are respectively realized by a radial spherical magnetic resistance MB and a pair of axial spherical magnetic resistance MBs. The 2-DOF deflections of the rotor are achieved by the Lorentz MB. To sense the real-time position of the rotor, the four radial eddy current displacement sensors are adopted for measuring the radial displacements, and the eight axial eddy current displacement sensors are used for detecting the axial displacements and the deflection angles. The displacement signals measured by the sensors are transported to the control system for adjusting the rotor attitude. In addition, the vacuum environment is kept by the three gyro houses. A pair of touchdown bearings is utilized to protect the rotor when the MBs are off or invalid.
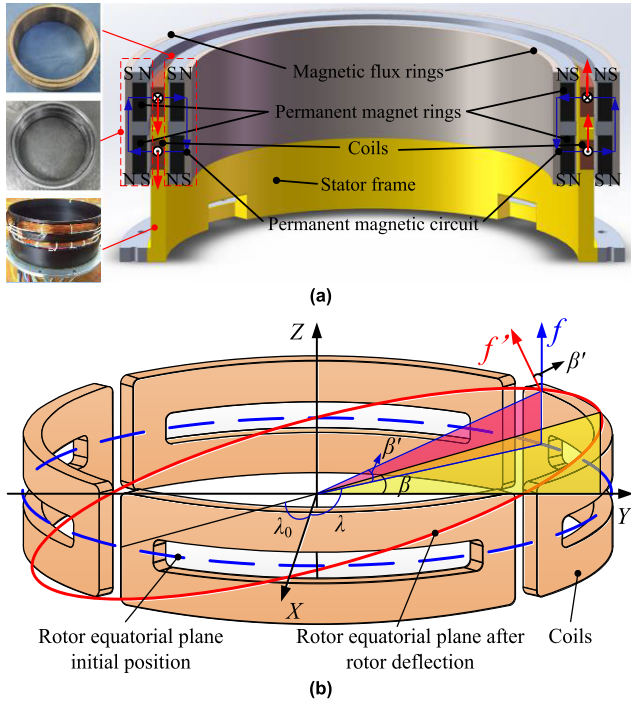
**(a)**



**(b)**

**FIGURE 2.** Lorentz MB: (a) Schematic diagram of Lorentz MB. (b) Change of ampere force direction when the rotor is tilted.

## III. THEORETICAL ANALYSIS OF 5-DOF DECOUPLING

### A. DECOUPLING BETWEEN 2-DOF DEFLECTIONS

In this VGMSFW, the structure of the Lorentz MB is shown in Figure 2a. The permanent magnet rings and the magnetic flux rings are fixed in the rotor edge slot. Four sets of the coils wound around the stator frame are placed in the air gap between the permanent magnet rings. The magnetic flux flowing across the four evenly distributed coils through two magnetic flux rings is produced by the four permanent magnet rings. The closed magnetic circuits plotted in the blue solid lines are got as the adjacent permanent magnet rings with opposite magnetization directions. The ampere forces for 2-DOF rotor deflection are generated by loading the control currents in coils.

There are two working modes of Lorentz MBs including the active vibration suppression and the torque output. In former mode, the high-frequency and small-amplitude torques are got to compensate the interference torque acting on the suspension rotor. In latter mode, the instantaneous large torque can be generated by actively tilting the high-speed rotor.

In Figure 2b, the ampere force generated by the coil current will be changed with the angle $\beta'$ when the rotor is tilted around X axis with deflection angle $\beta$. The angle $\beta'$ can be expressed as,

$$\beta' = \arcsin\left(\sin\lambda\sin\beta\right) \quad (1)$$

where $\lambda$ is the longitude angle of coils. The ampere force microelements $d\boldsymbol{f_{up}}$ and $d\boldsymbol{f_{down}}$ respectively produced by the upper and lower coils can be analytically got based on the

Ampere's rule, which can be written as,

$$d\boldsymbol{f_{up}} = d\boldsymbol{f_{down}} = nBi_l r \begin{bmatrix} -\cos\lambda\sin\beta' \\ -\sin\lambda\sin\beta' \\ \cos\beta' \end{bmatrix} d\lambda \quad (2)$$

where $n$ is the number of the coil turns, $B$ is the air gap magnetic flux density, $i_l$ is the control current in the Lorentz MB coils, and $r$ is the radius of the coils. Therefore, the deflection torque microelement $d\boldsymbol{T_{up}}$ and $d\boldsymbol{T_{down}}$ can be obtained as,

$$d\boldsymbol{T_{up}} = \boldsymbol{r_{up}} \times d\boldsymbol{f_{up}}$$
$$= nBi_l r \begin{bmatrix} r\sin\lambda\cos\beta' + a\sin\lambda\sin\beta' \\ -a\cos\lambda\sin\beta' - r\cos\lambda\cos\beta' \\ 0 \end{bmatrix} d\lambda \quad (3)$$

$$d\boldsymbol{T_{down}} = \boldsymbol{r_{down}} \times d\boldsymbol{f_{down}}$$
$$= nBi_l r \begin{bmatrix} r\sin\lambda\cos\beta' d\lambda - a\sin\lambda\sin\beta' d\lambda \\ a\cos\lambda\sin\beta' d\lambda - r\cos\lambda\cos\beta' d\lambda \\ 0 \end{bmatrix} \quad (4)$$

where, $\boldsymbol{r_{up}}$ and $\boldsymbol{r_{down}}$ are the force arms of the upper and lower coils, which can be given by,

$$\begin{cases} \boldsymbol{r_{up}} = r\cos\lambda\boldsymbol{X_0} + r\sin\lambda\boldsymbol{Y_0} + a\boldsymbol{Z_0} \\ \boldsymbol{r_{down}} = r\cos\lambda\boldsymbol{X_0} + r\sin\lambda\boldsymbol{Y_0} - a\boldsymbol{Z_0} \end{cases} \quad (5)$$

where $\boldsymbol{X_0}$, $\boldsymbol{Y_0}$ and $\boldsymbol{Z_0}$ are the unit vectors in the X, Y, Z directions, and $a$ is half the axial height of the coils. According to (3) and (4), the torque microelement $d\boldsymbol{T}$ generated by a set of coils can be integrated as,

$$d\boldsymbol{T} = d\boldsymbol{T_{up}} + d\boldsymbol{T_{down}} = 2nBi_l r^2 \begin{bmatrix} \sin\lambda\cos\beta' \\ -\cos\lambda\cos\beta' \\ 0 \end{bmatrix} d\lambda \quad (6)$$

When the two control currents with the same value $i_{ly}$ and the opposite directions are loaded in the two sets of coils in the Y direction, a pair of ampere forces with the same value and opposite directions are generated to drive the rotor deflection around X axis. The deflection torque $\boldsymbol{T_x}$ around X axis is written as,

$$\boldsymbol{T_x} = 8nBi_{ly}r^2 \begin{bmatrix} \frac{1}{3}\sin^2\beta\sin^3\lambda_0 + \cos^2\beta\sin\lambda_0 \\ 0 \\ 0 \end{bmatrix} \quad (7)$$

where $\lambda_0$ is the half of the center angle of single coil. Similarly, when the two control currents with the same value $i_{lx}$ and opposite directions are applied to the two sets of coils in the X direction, the deflection torque $\boldsymbol{T_y}$ around Y axis is presented as,

$$\boldsymbol{T_y} = 8nBi_{lx}r^2 \begin{bmatrix} 0 \\ \frac{1}{3}\sin^2\beta\sin^3\lambda_0 + \sin\lambda_0 \\ 0 \end{bmatrix} \quad (8)$$

According to (7) and (8), the control currents in ±X direction are only utilized for generating the deflection torques around Y axis, and the control currents in ±Y direction are only used for producing the deflection torques around X axis. It indicates that the 2-DOF deflections of the Lorentz

**TABLE 1.** Design parameters of the LORENTZ MB.

| Symbol | Quantity | Value |
|--------|----------|-------|
| $n$ | Number of the coil turns | 200 |
| $B$ | Air gap magnetic flux density | 0.4 T |
| $r$ | Coils radius | 58.85 mm |
| $\lambda_0$ | Half of the center angle of single coil | 42 degree |
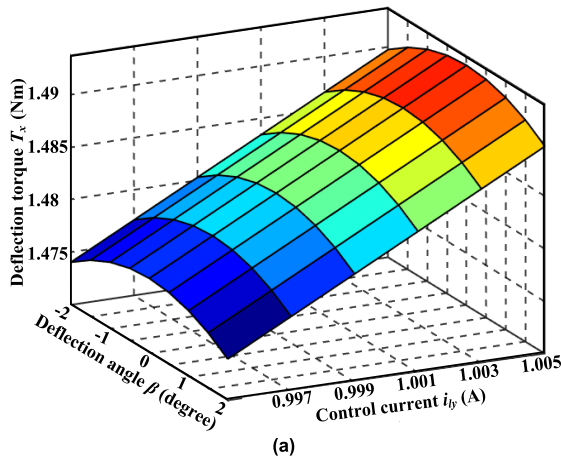


**(a)**
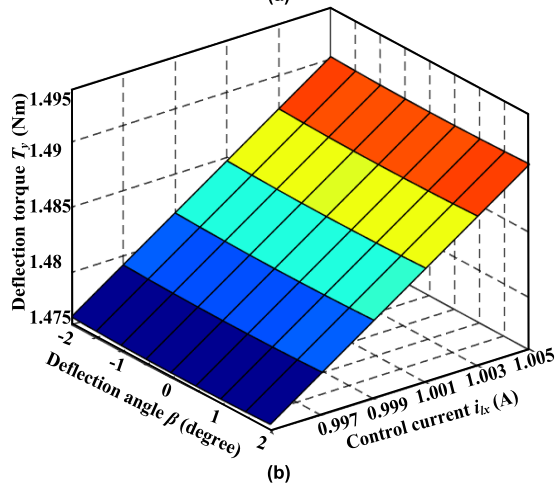


**(b)**

**FIGURE 3.** Deflection torque versus deflection angle and control current: (a) Deflection torque $T_x$ versus deflection angle $\beta$ and control current $i_{ly}$. (b) Deflection torque $T_y$ versus deflection angle $\beta$ and control current $i_{lx}$.

MB are decoupled whether the rotor is tilted. Based on the design parameters listed in Table 1, the relationship of the deflection torques versus the rotor deflection angle and the control current is shown in Figure 3.

As shown in Figure 3a and 3b, when the rotor is tilted around the X axis within $\pm 2°$, the change of the deflection torque $T_y$ is obviously less than that of the deflection torque $T_x$ under the same excitation current. Similarly, when the rotor is tilted around the Y axis within $\pm 2°$, the deflection torque $T_y$ will be obviously changed compared with the deflection torque $T_x$ with constant value. In Figure 3a, the variation range of the deflection torque $T_x$ is less than 2 mNm, which is far less than itself about 1.47 Nm. Thus, the deflection torque is approximately linear with the control current, and the current stiffness is about 1.5 Nm/A. Based on
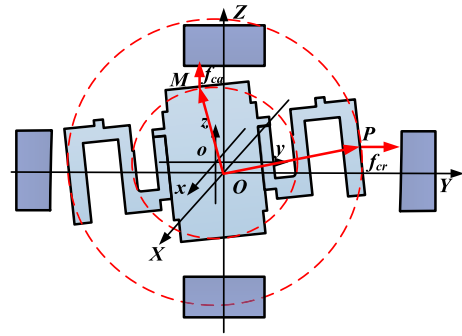


**FIGURE 4.** Air gap mathematical model of the cylinder magnetic resistance MBs-rotor system.

the analysis above, the high-precision deflections of the rotor are realized by precisely controlling the currents in the coils.

### B. DECOUPLING BETWEEN TRANSLATION AND DEFLECTION

According to the Maxwell electromagnetic suction equation [21], the electromagnetic force $f$ generated by the magnetic resistance MB stator is given by,

$$f = \frac{\phi^2}{2\mu_0 A} = \frac{\mu_0 A N^2 i^2}{2g^2} \tag{9}$$

where $\Phi$ is the total magnetic flux generated by the magnetic resistance MB, $\mu_0$ is the vacuum permeability, $A$ is the area of magnetic pole, $N$ is the number of the coil turns, $i$ is the control current in coils, and $g$ is the air gap between the magnetic pole and the rotor.

The mathematical models of air gap are established for analyzing the effect of the rotor motions on electromagnetic forces. The air gap model of the conventional cylindrical magnetic resistance MBs-rotor system is shown in Figure 4. $O$ is the stator center of the magnetic resistance MBs and $P$ is the arbitrary point on the rotor rim. When the rotor is offset from point $O$ to point $o$, and tilted around the X axis with deflection angle $\beta$, $\boldsymbol{OP}$ can be expressed as,

$$\boldsymbol{OP} = \begin{bmatrix} 1 & 0 & 0 \\ 0 & \cos\beta & -\sin\beta \\ 0 & \sin\beta & \cos\beta \end{bmatrix} \begin{bmatrix} e_x + r_c\cos\theta \\ e_y + r_c\sin\theta \\ e_z + z \end{bmatrix}$$

$$= \begin{bmatrix} e_x + r_c\cos\theta \\ (e_y + r_c\sin\theta)\cos\beta - (e_z + z)\sin\beta \\ (e_y + r_c\sin\theta)\sin\beta + (e_z + z)\cos\beta \end{bmatrix} \tag{10}$$

where $e_x$, $e_y$ and $e_z$ are respectively the rotor offset components along the X, Y, Z directions, $\theta$ is the latitude angle of the point $P$, $r_c$ is the radius of the cylindrical rotor and $z$ is the half of the rotor rim height. The radial air gap $g_{cr}$ can be calculated as, (11) shown at the bottom of next page, where $R_c$ is the radius of the cylindrical magnetic resistance MB stator. Similarly, the axial air gap $g_{ca}$ is written as,

$$g_{ca} = R_a - |proj_{PlaneXOZ}(\boldsymbol{OM})|$$
$$= R_a - e_y - e_z - r\sin\theta\cos\beta - z_0\sin\beta \tag{12}$$

where $R_a$ is the half the distance between the stator magnetic poles of the two axial magnetic resistance MBs, $M$ is the arbitrary point on the end of the rotor shaft, $r$ is the distance in XOY between the point $O$ and the point $M$ on the end of the rotor shaft, and $z_0$ is the half the axial height of cylindrical rotor. When the rotor is tilted only around the X axis, the deflection interference torques $\boldsymbol{T_{cr}}$ and $\boldsymbol{T_{ca}}$ generated by the radial and axial magnetic resistance MBs are given by,

$$
\begin{cases}
\boldsymbol{T_{cr}} = 2\boldsymbol{f_{cr}} \times \boldsymbol{OP} \\
= 2\iint\limits_{s} \left( \frac{\mu_0 A N_{cr}^2 i_{cr}^2}{\left( R_c - \sqrt{(r_c \cos\theta)^2 + (r_c \sin\theta\cos\beta - z\sin\beta)^2} \right)^2} \cdot \begin{bmatrix} \sin\theta\,(r_c\sin\theta\sin\beta + z\cos\beta) \\ -\cos\theta\,(r_c\sin\theta\sin\beta + z\cos\beta) \\ \cos\theta\,(r_c\sin\theta\cos\beta - z\sin\beta - r_c\sin\theta) \end{bmatrix} \right) ds \\
\boldsymbol{T_{ca}} = 2\boldsymbol{f_{ca}} \times \boldsymbol{OM} \\
= 2\iint\limits_{s} \left( \frac{\mu_0 A N_{ca}^2 i_{ca}^2}{(R_a - e_y - e_z - r\sin\theta\cos\beta - z_0\sin\beta)^2} \cdot \begin{bmatrix} z_0\sin\beta - r\sin\theta\cos\beta \\ r\cos\theta \\ 0 \end{bmatrix} \right) ds
\end{cases}
$$

(13)

where $\boldsymbol{f_{cr}}$ and $\boldsymbol{f_{ca}}$ are the electromagnetic forces generated by the cylindrical radial and axial magnetic resistance MBs, which can be expressed as,

$$
\begin{cases}
\boldsymbol{f_{cr}} = \dfrac{\mu_0 A N_{cr}^2 i_{cr}^2}{g_{cr}^2} \cdot \begin{bmatrix} \cos\theta & \sin\theta & 0 \end{bmatrix}^T \\
\boldsymbol{f_{ca}} = \dfrac{\mu_0 A N_{ca}^2 i_{ca}^2}{g_{ca}^2} \cdot \begin{bmatrix} 0 & 0 & 1 \end{bmatrix}^T
\end{cases}
$$

(14)

where $N_{cr}$ and $N_{ca}$ are the number of the coil turns of the cylindrical radial and axial MBs, and $i_{cr}$ and $i_{ca}$ are the coil control currents in cylindrical radial and axial MBs.

The rotor is tilted around the X axis with angle 1.5°. The design parameters of the VGMSFW are substituted into (13). The interference torques $\boldsymbol{T_{cr}}$ and $\boldsymbol{T_{ca}}$ along +X direction are about 0.06 Nm and 0.05 Nm, respectively. Both of them are larger than 3% of the deflection torque $\boldsymbol{T_x}$ about 1.47 Nm. Similarly, the rotor deflection interference torques around the Y axis can be obtained. Based on the analysis above, the interference torques generated by the magnetic resistance MBs are the main factor affecting the deflection control precision under the rotor deflection.

To remedy the limitation of cylindrical magnetic resistance MB with the large interference torque, the spherical magnetic resistance MB is presented. The MBs-rotor system is built
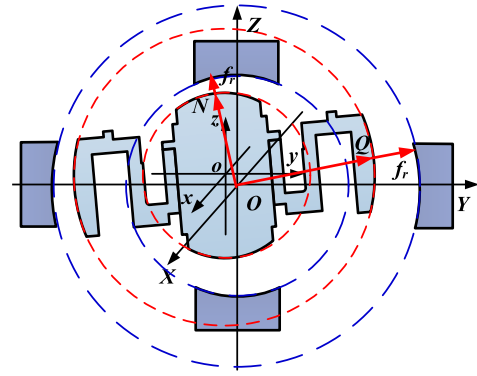
in Figure 5. Similar to the motions in Figure 4, the sphere rotor is driven from the stator center $O$, and the vector $\boldsymbol{OQ}$ between the stator center $O$ and arbitrary point $Q$ on the sphere rotor rim is written as,

$$
\boldsymbol{OQ} = \begin{bmatrix} 1 & 0 & 0 \\ 0 & \cos\beta & -\sin\beta \\ 0 & \sin\beta & \cos\beta \end{bmatrix} \begin{bmatrix} e_x + r_s\sin\theta\cos\varphi \\ e_y + r_s\sin\theta\sin\varphi \\ e_z + r_s\cos\theta \end{bmatrix}
$$
$$
= \begin{bmatrix} e_x + r_s\sin\theta\cos\varphi \\ (e_y + r_s\sin\theta\sin\varphi)\cos\beta - (e_z + r_s\cos\theta)\sin\beta \\ (e_y + r_s\sin\theta\sin\varphi)\sin\beta + (e_z + r_s\cos\theta)\cos\beta \end{bmatrix}
$$

(15)

where $r_{sr}$ is the radial radius of the sphere rotor, $\theta$ and $\varphi$ are the latitude and longitude angle of the point $Q$. The radial air gap $g_{sr}$ is obtained as, (16) shown at the bottom of next page, where $R_{sr}$ is the radius of the spherical radial magnetic resistance MB stator. Similarly, the axial air gap $g_{sa}$ can be expressed as, (17) shown at the bottom of next page, where $R_{sa}$ is the radius of the spherical axial magnetic resistance MB stator, and $r_{sa}$ is the axial radius of the sphere rotor. It can be seen in (16) and (17) that there is irrelevance between the air gap and the deflection angle. So no interference torques occur when the rotor is tilted, and the rotor decoupling between the translation and the deflection is realized.

## C. DECOUPLING AMONG 3-DOF TRANSLATIONS

The radial/axial spherical magnetic resistance MBs are utilized to support the rotor, and the MBs-rotor system is shown in Figure 6. Two axial spherical magnetic resistance MBs are located at the upper and lower ends of the spherical rotor. The four stator cores with two magnetic poles are placed circumferentially in the ±X and ±Y directions. The eddy current loss in radial direction is far larger than that in axial direction, as the obvious change of the radial air gap

$$
g_{cr}
$$
$$
= R_c - |proj_{PlaneXOY}(\boldsymbol{OP})| = R_c - \sqrt{(e_x + r_c\cos\theta)^2 + ((e_y + r_c\sin\theta)\cos\beta - (e_z + z)\sin\beta)^2}
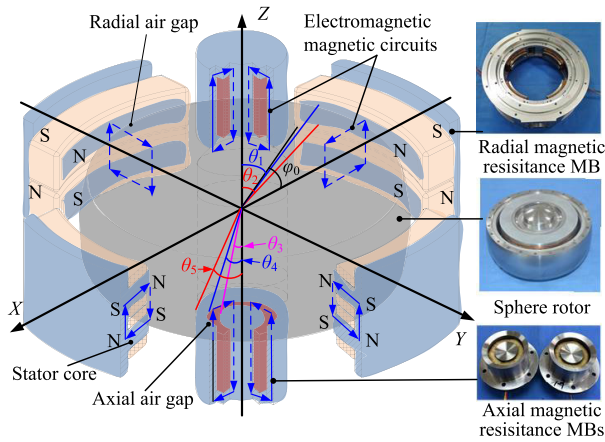$$

(11)

**FIGURE 6.** Radial/axial spherical magnetic resistance MBs-rotor system.

magnetic flux density when the rotor rotates. To decrease the radial eddy current loss, the homopolar radial MB is adopted. As shown in Figure 6, the four upper magnetic poles with the same polarities are opposite to the four lower magnetic poles.

The rotor is offset along +X direction with $e_x$. According to (16) and (17), the radial and axial air gaps $g_{sr}$ and $g_{sa}$ are given by,

$$\begin{cases} g_{sr} = R_{sr} - \sqrt{e_x^2 + r_{sr}^2 + 2r_{sr}e_x \sin\theta \cos\varphi} \\ g_{sa} = R_{sa} - \sqrt{e_x^2 + r_{sa}^2 + 2r_{sa}e_x \sin\theta \cos\varphi} \end{cases} \quad (18)$$

Based on (9) and (18), the resultant force $f_x$ in X direction generated by radial magnetic resistance MB can be got as,

$$\begin{aligned} \boldsymbol{f}_x &= \boldsymbol{f}_{x+} + \boldsymbol{f}_{x-} \\ &= 2\int_{-\varphi_0}^{\varphi_0} \int_{\theta_1}^{\theta_2} \left( \frac{\mu_0 N_r^2 R_{sr}^2 (i_{rb} - i_{rx})^2}{\sigma_r g_{sr}^2 (e_x, \theta, \varphi)} \right. \\ &\quad \left. - \frac{\mu_0 N_r^2 R_{sr}^2 (i_{rb} + i_{rx})^2}{\sigma_r g_{sr}^2 (-e_x, \theta, \varphi)} \right) \sin^2\theta \cos\varphi d\varphi d\theta \quad (19) \end{aligned}$$

where $\varphi_0$ is the half of the center angle of a single magnetic pole in XOY, $\theta_1$ and $\theta_2$ are the latitude angles of the single magnetic pole upper and lower edges, $N_r$ is the number of the coil turns, $i_{rb}$ is the bias current for keeping the rotor stably suspending in radial direction, $i_{rx}$ is the coil control current in X direction, and $\sigma_r$ is the electromagnetic flux leakage coefficient of the radial MB. As shown in (19), the resultant force $f_x$ is only related to the offset $e_x$ and the control current $i_{rx}$. Similarly, the resultant force $\boldsymbol{f}_y$ in Y direction only related to the offset $e_y$ and the coil control current in Y direction $i_{ry}$ is obtained, when the rotor is offset along +Y direction with $e_y$. If the rotor is offset along +Z direction

with $e_z$, the radial and axial air gap are written as,

$$\begin{cases} g_{sr} = R_{sr} - \sqrt{e_z^2 + r_{sr}^2 + 2r_{sr}e_z \cos\theta} \\ g_{sa} = R_{sa} - \sqrt{e_z^2 + r_{sa}^2 + 2r_{sa}e_z \cos\theta} \end{cases} \quad (20)$$

The resultant force $f_z$ in Z direction generated by two axial magnetic resistance MBs can be given by,

$$\begin{aligned} \boldsymbol{f}_z &= \boldsymbol{f}_{z+} + \boldsymbol{f}_{z-} \\ &= \int_0^{2\pi} \int_0^{\theta_3} \left( \frac{\mu_0 N_a^2 (i_{ab} - i_{az})^2 R_{sa}^2}{\sigma_a g_{sa}^2 (e_z, \theta, \varphi)} \right. \\ &\quad \left. - \frac{\mu_0 N_a^2 (i_{ab} + i_{az})^2 R_{sa}^2}{\sigma_a g_{sa}^2 (-e_z, \theta, \varphi)} \right) \sin^2\theta d\varphi d\theta \\ &\quad + \int_0^{2\pi} \int_{\theta_4}^{\theta_5} \left( \frac{\mu_0 N_a^2 (i_{ab} - i_{az})^2 R_{sa}^2}{\sigma_a g_{sa}^2 (e_z, \theta, \varphi)} \right. \\ &\quad \left. - \frac{\mu_0 N_a^2 (i_{ab} + i_{az})^2 R_{sa}^2}{\sigma_a g_{sa}^2 (-e_z, \theta, \varphi)} \right) \sin^2\theta d\varphi d\theta \quad (21) \end{aligned}$$

where $\theta_3$ is the half of the latitude angle of the inner magnetic pole, $\theta_4$ and $\theta_5$ are the half of the latitude angles of the inner and outer edge of the outer magnetic pole, $N_a$ is the number of the axial MB coil turns, $i_{ab}$ is the bias current for keeping the rotor stably suspending in axial direction, $i_{az}$ is the coil control current of the upper and lower axial MBs, and $\sigma_a$ is electromagnetic flux leakage coefficient of the axial MBs. The resultant force $f_z$ is only determined by the offset $e_z$ and the control current $i_{az}$. Based on the analysis above, the decoupling among the 3-DOF translations is realized whether the rotor is offset.

The design parameters are listed in Table 2. The force-displacement and force-current characteristics of the magnetic resistance MBs are plotted in Figure 7. It can be seen in Figure 7a that the force-current stiffness and force-displacement stiffness of radial MB are 387.1N/A and −553.1N/mm. As shown in Figure 7b, the force-current stiffness and force-displacement stiffness of axial MBs are 580.5N/A and −829.3N/mm, respectively.

## IV. EXPERIMENT AND ANALYSIS
### A. SPHERE ROTOR DYNAMICS MODEL AND CONTROL SYSTEM
When the rotor is suspended stably, the forces and torques acting on the sphere rotor are shown in Figure 8. $f_x$, $f_y$ and $f_z$ are the translation electromagnetic forces generated by the radial and axial magnetic resistance MBs. $T_x$ and $T_y$ are the deflection torques around X and Y axes. According

$$g_{sr} = R_{sr} - |\boldsymbol{OQ}| = R_{sr} - \sqrt{e_x^2 + e_y^2 + e_z^2 + r_{sr}^2 + 2r_{sr}\left(e_x \sin\theta \cos\varphi + e_y \sin\theta \sin\varphi + e_z \cos\theta\right)} \quad (16)$$

$$g_{sa} = R_{sa} - |\boldsymbol{OQ}| = R_{sa} - \sqrt{e_x^2 + e_y^2 + e_z^2 + r_{sa}^2 + 2r_{sa}\left(e_x \sin\theta \cos\varphi + e_y \sin\theta \sin\varphi + e_z \cos\theta\right)} \quad (17)$$

**TABLE 2.** Design parameters of the radial/axial magnetic resistance MBs.

| Symbol | Value | Symbol | Value |
|--------|-------|--------|-------|
| $R_{sr}$ | 78.35 mm | $R_{sa}$ | 41.7 mm |
| $r_{sr}$ | 78 mm | $r_{sa}$ | 41.35 mm |
| $N_r$ | 200 | $N_a$ | 560 |
| $\sigma_r$ | 1.04 | $\sigma_a$ | 1.05 |
| $\varphi_1$ | 26 deg | $\theta$ | 89 deg |
| $\theta_2$ | 101 deg | $\theta_3$ | 13 deg |
| $\theta_4$ | 20 deg | $\theta_5$ | 25 deg |
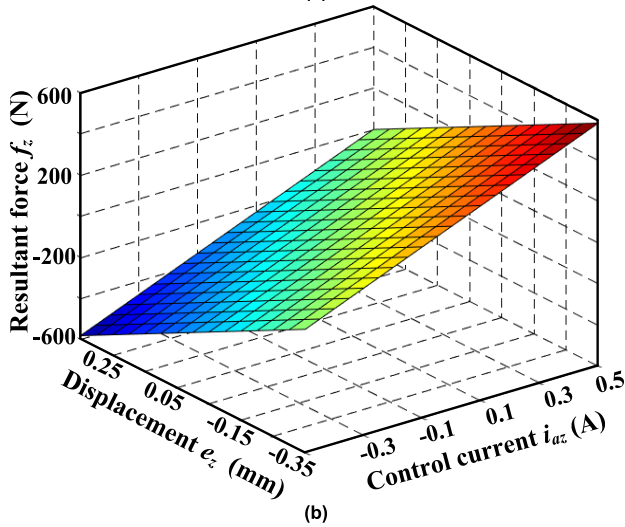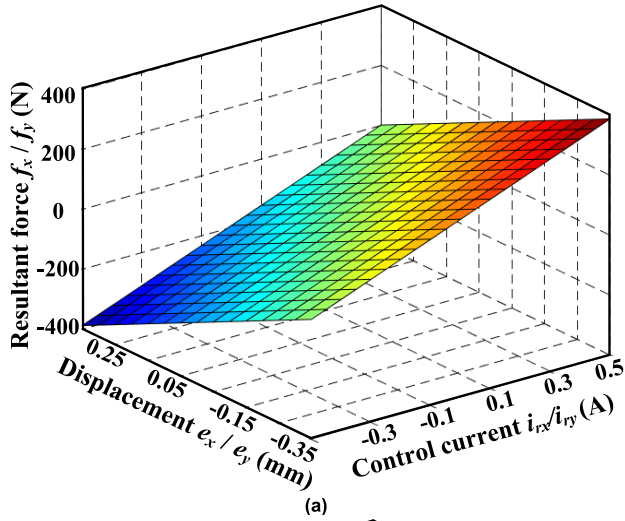




**FIGURE 7.** Force-displacement and force-current characteristics of the radial and axial magnetic resistance MBs: (a) Resultant force $f_x / f_y$ in X/Y directions versus offset $e_x/e_y$ in X/Y directions and control current $i_{rx}/i_{ry}$. (b) Resultant force $f_z$ in Z direction versus offset $e_z$ in Z axis direction and control current $i_{rz}$.

to the Newton's second law and the gyro-kinetic equation, the dynamic model of the rotor system can be integrated as,

$$
\begin{cases}
m\ddot{x} = k_{ir}i_{rx} + k_{er}x \\
m\ddot{y} = k_{ir}i_{ry} + k_{er}y \\
m\ddot{z} = k_{ia}i_{az} + k_{ea}z \\
J_x\ddot{\beta} - J_z\omega\dot{\gamma} = k_{il}i_x \\
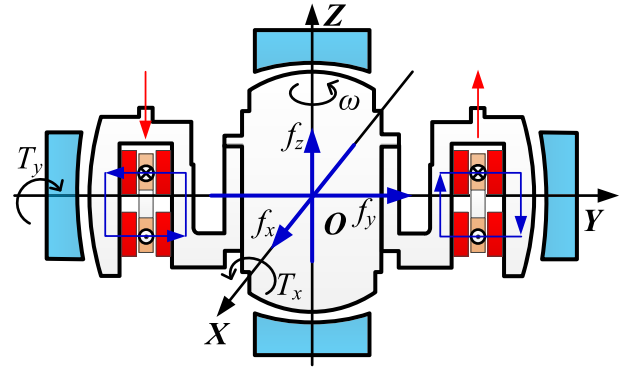J_y\ddot{\gamma} + J_z\omega\dot{\beta} = k_{il}i_y
\end{cases}
\tag{22}
$$

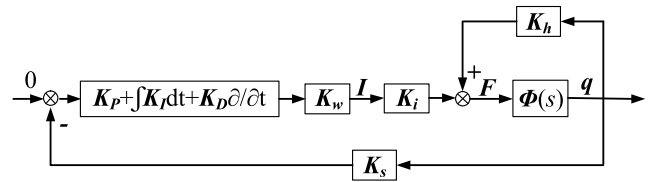

**FIGURE 8.** Force analysis of VGMSFW rotor system.
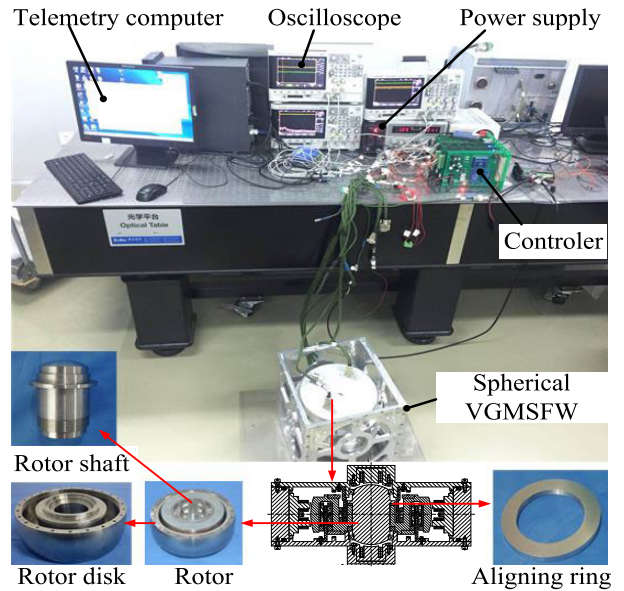


**FIGURE 9.** VGMSFW control system.



**FIGURE 10.** Development of prototype and establishment of experimental platform.

where $m$ is the rotor mass, $J_x$, $J_y$ and $J_z$ are the rotary inertial momentum around X, Y and Z axes, $x$, $y$, $z$ are the rotor displacements along X, Y and Z directions, $\beta$ and $\gamma$ are the rotor deflection angles around X and Y axes, $k_{ir}$ and $k_{ia}$ are the force-current stiffnesses of radial and axial magnetic resistance MBs, $k_{er}$ and $k_{ea}$ are the force-displacement stiffnesses of radial and axial magnetic resistance MBs, $k_{il}$ is the torque-current stiffness of the Lorentz MB, and $\omega$ is the rotor rotating speed. Equation (22) can be rewritten in the form
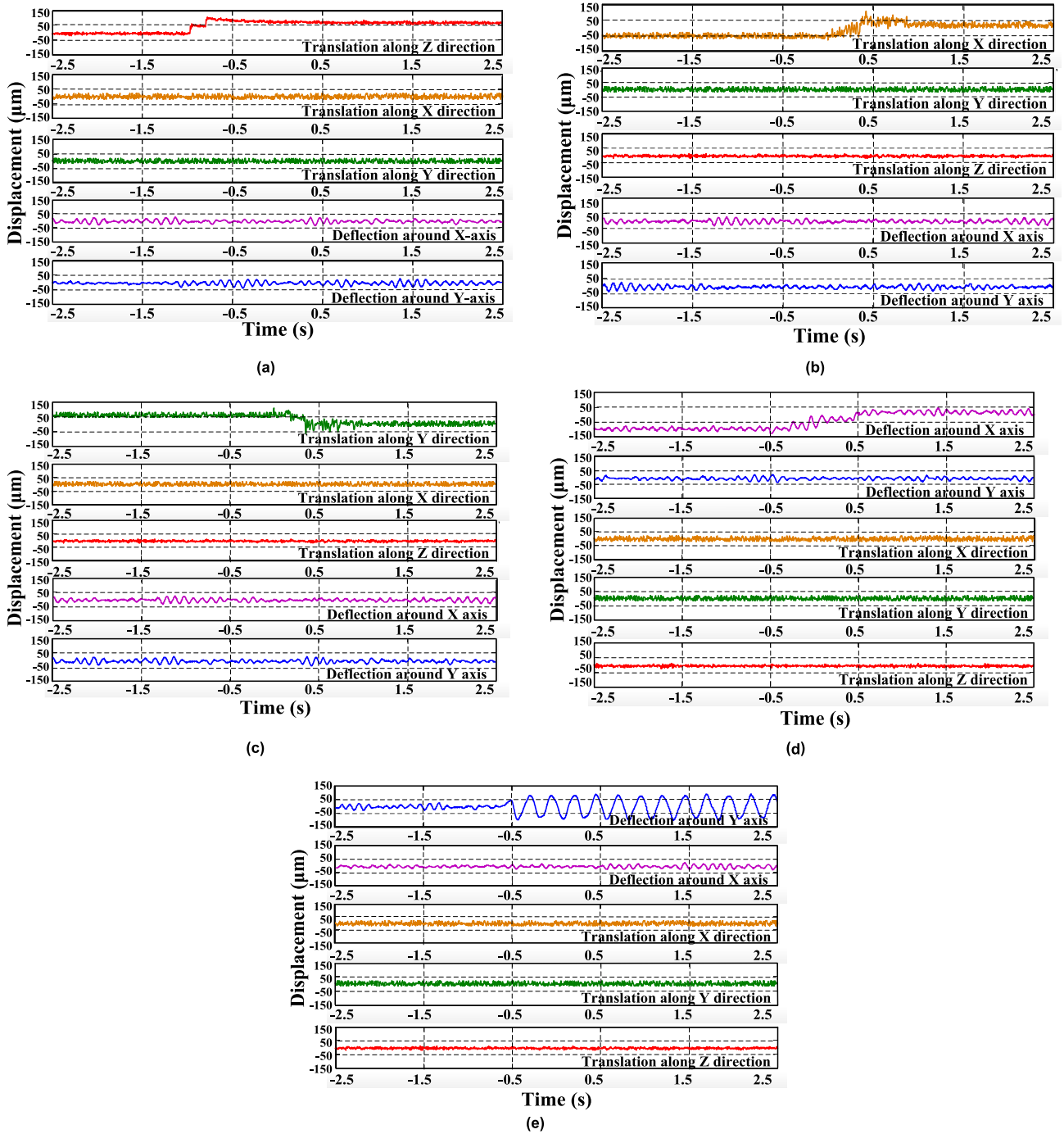
**FIGURE 11.** Decoupling experiment of the spherical VGMSFW: (a) Step signal applied to axial translation channel. (b) Step signal applied to radial X-axis translation channel. (c) Step signal applied to radial Y-axis translation channel. (d) Step signal applied to deflection channel around X axis. (e) Sine signal applied to deflection channel around Y axis.

of matrix,

$$M\ddot{q} + K_c\dot{q} - K_dq = K_iI \quad (23)$$

where, the mass matrix $M=$ diag $(m, m, m, J_x, J_y)$, the displacement matrix $q= [x, y, z, \beta, \gamma]^T$, the coupling matrix

$K_c = \begin{bmatrix} \mathbf{0}_{3\times3} & \mathbf{0}_{3\times1} & \mathbf{0}_{3\times1} \\ \mathbf{0}_{1\times3} & 0 & -1 \\ \mathbf{0}_{1\times3} & 1 & 0 \end{bmatrix} J_z\omega,$ the displacement stiffness matrix $K_d =$ diag $(k_{er}, k_{er}, k_{ea}, 0, 0)$, the current stiffness matrix $K_i = [k_{ir}, k_{ir}, k_{ia}, k_{il}, k_{il}]^T$, and the control current matrix $I= [i_{rx}, i_{ry}, i_{az}, i_x, i_y]^T$. Based on the dynamic

**TABLE 3. Control parameters of the VGMSFW.**

| Symbol | Quantity | Value |
|--------|----------|-------|
| $m$ | Rotor mass | 6 kg |
| $J_x$ | Rotary inertial momentum around X axis | 0.0097 kg·m$^2$ |
| $J_y$ | Rotary inertial momentum around Y axis | 0.0097 kg·m$^2$ |
| $J_z$ | Rotary inertial momentum around Z axis | 0.0167 kg·m$^2$ |
| $\omega$ | Rotor rotating speed | 8000 r/min |
| $k_{er}$ | Force-displacement stiffness of the radial MB | -553.1 N/mm |
| $k_{ea}$ | Force-displacement stiffness of the axial MBs | -829.3 N/mm |
| $k_{ir}$ | Force-current stiffness of the radial MB | 387.1 N/A |
| $k_{ia}$ | Force-current stiffness of the axial MBs | 580.5 N/A |
| $k_{il}$ | Torque-current stiffness of the Lorentz MB | 1.5 N/A |
| $K_s$ | Sensitivity of the sensor | 10 V/mm |
| $K_w$ | Amplification coefficient | 0.22 |

model, the control system is designed, which is shown in Figure 9. Where, $F$= diag $(f_x, f_y, f_z, T_x, T_y)$ is the force matrix, $\Phi(s) = (Ms^2 + K_c s)^{-1}$ is transfer function of the control system, $K_w$ and $K_s$ are respectively the amplification coefficient and the sensor sensitivity.

## B. EXPERIMENTAL SETUP

The prototype of the VGMSFW is manufactured. The three rotor spherical surfaces with the sphericity of 3 $\mu$m and the spherical surface roughness of 0.1 $\mu$m are machined by the mesh grinding method. The coincidence between the sphere center and the rotor centroid is realized by adjusting the thickness of the aligning ring. The on-line dynamic balance test is carried out, and the unbalanced mass of the sphere rotor is compensated by the counterweight screws in the upper and lower counterweight surfaces. The experimental platform of VGMSFW is shown in Figure 10, and the control parameters are listed in Table 3. The control current is supplied to the MBs through the power amplifier. Based on the CAN bus, the real-time control and monitoring of the system are realized by the telemetry computer.

## C. DECOUPLING EXPERIMENT

To verify the performance of the spherical VGMSFW, the decoupling experiments of the prototype are implemented. When the rotor is stably suspended, the step or sine current signal is applied to the arbitrary channel of the VGMSFW system, and the displacement fluctuation curves of the other channels are plotted in Figure 11.

As shown in Figure 11a, the sphere rotor is offset along +Z direction with 50 $\mu$m due to the step signal applied to the axial channel. The radial displacement amplitude is 20 $\mu$m. The deflection displacement amplitude is 30 $\mu$m, and its corresponding deflection angle is 0.036°. Both the radial and deflection displacements are almost unchanged. It can be seen in Figure 11b and Figure 11c that, when the step signals are respectively loaded into the X and Y translation channels, the sphere rotor is respectively offset along +X and +Y direction with ±50 $\mu$m, the displacements in the other channels are constant. The radial and axial rotor amplitudes are respectively less than 20 $\mu$m and 12 $\mu$m, and
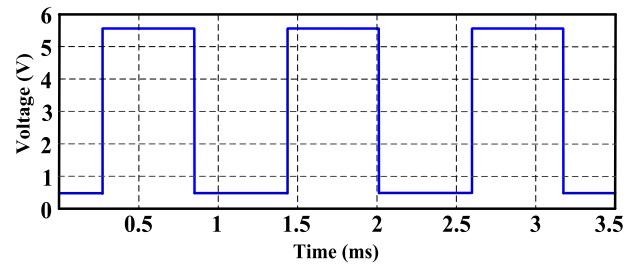


**FIGURE 12. Hall output waveform under rated speed.**
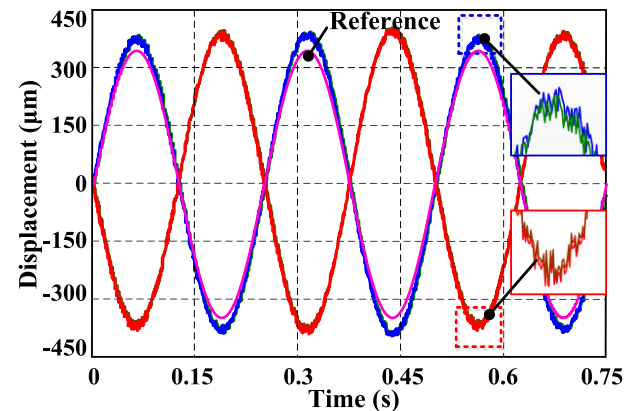


**FIGURE 13. Displacements measured by the four axial sensors in Y direction when the sphere rotor deflects around X axis.**

the deflection displacement amplitudes are within 30 $\mu$m with corresponding deflection angle of 0.036°. It indicates that there is no interference between the 3-DOF translations decoupled mutually and 2-DOF deflections. Similarly, the step and sine signals are respectively applied to the deflection channels around X and Y axes. There is no obvious displacement variation in other four channels, which can be seen in Figure 11d and Figure 11e. The interference of 2-DOF deflections to 3-DOF translations can be ignored, and the decoupling between the 2-DOF deflections is realized. Therefore, the 5-DOF motions of the spherical VGMSFW can be considered as decoupling mutually. That is accordance with the theoretical analysis in part III, which provides the basis for the high-precision and stable control of the rotor.

## D. TORQUE EXPERIMENT

As the decoupling among the 5-DOF motions of the sphere rotor, the high-precision gyroscopic moment $M_{gyro}$ can be obtained by tilting high speed sphere rotor, which can be expressed as,

$$M_{gyro} = -J_z \omega \times \Omega \qquad (24)$$

where $\omega$ and $\Omega$ are the rated speed and the procession angular velocity of the sphere rotor. The rotor rated speed is measured by the Hall switch sensors in the motor stator. The speed measurement waveform with the period of 1.25 ms is plotted in Figure 12, and the measurement frequency $f_m$ about
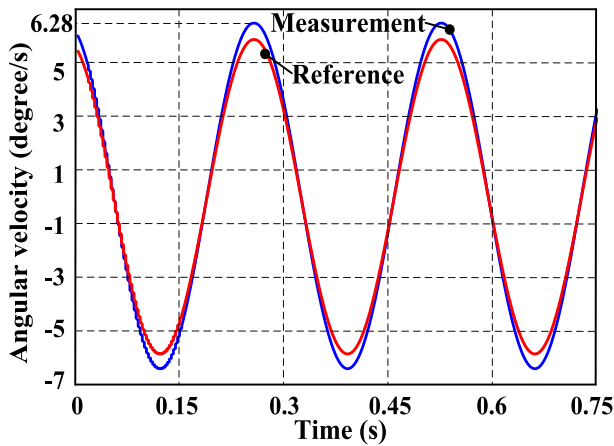
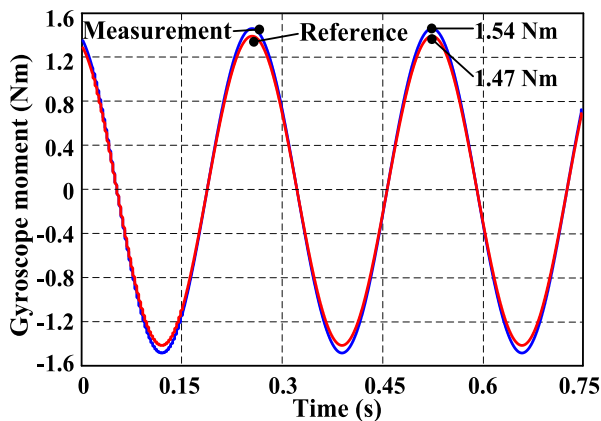**FIGURE 14.** Procession angular velocity curve of the sphere rotor.



**FIGURE 15.** Gyroscope moment of the spherical VGMSFW.

801.9 Hz is got. Since the six pairs of the motor magnetic poles, the rated speed is about 8019 r/min corresponding to the speed accuracy of 2.4 r/min.

The sine signal with amplitude of 350 $\mu$m and frequency of 4 Hz is loaded into the Lorentz MB coils in Y direction. The axial displacement responses measured by the four axial sensors in $\pm$Y directions are shown in Figure 13. The difference method is used for calculating the axial displacement. The procession angular velocity is got by taking the derivate of the terminal displacement curve, which is shown in Figure 14. The measurement and reference curves of the procession angular velocity are plotted in the blue and red solid line. The maximum measurement/reference angular velocities are respectively about 6.28 °/s and 6 °/s. Thus, the procession angular velocity accuracy of the sphere rotor is about 0.047 °/s, which is better than that about 0.32 °/s of the VGMSFW with conical MB in [28].

Based on (24), the curves of the gyroscopic moment generated by the sphere rotor are plotted in Figure 15. When the procession angular velocity of the rated speed rotor is at the maximum, the maximum actual and reference gyroscopic moments are about respectively 1.54 Nm and 1.47 Nm, and

its corresponding accuracy is about 0.048 Nm. Therefore, the high-precision agile maneuver of the spacecraft can be achieved by the spherical VGMSFW.

## V. CONCLUSION
In this paper, a 5-DOF decoupled spherical VGMSFW is developed for spacecrafts. Its structure and principle are introduced. The electromagnetic force models of the Lorentz MB and magnetic resistance MBs are built, and the decoupling among 5-DOF motions is demonstrated by the numerical analysis method. The spherical VGMSFW control system is established, and the decoupling and torque experiments are carried out based on the prototype. The decoupling among the 5-DOF motions is verified by the decoupling experiment. The torque experiment results show that the maximum gyroscopic moment about 1.54 Nm and its corresponding moment accuracy about 0.048 Nm are obtained when the sphere rotor is actively tilted. Both the two experiments indicate that the high-precision control and agile maneuver requirements for spacecraft can be effectively fulfilled by the novel spherical VGMSFW.

## REFERENCES
[1] J. G. Bitterly, "Flywheel technology: Past, present, and 21st century projections," *IEEE Aerosp. Electron. Syst. Mag.*, vol. 13, no. 8, pp. 13–16, Aug. 1998.
[2] B. Penne, C. Tobehn, M. Kassebom, and B. Ziegler, "A high agile satellite platform for Earth Observation—Performance description using new generation missions," in *Proc. 57th Int. Astronaut. Congr.*, Valencia, Spain, Oct. 2006, pp. 1–7.
[3] L. Qiang, W. Kun, R. Yuan, C. Xiaocen, M. Limei, and Z. Yong, "Optimization design of launch locking protective device (LLPD) based on carbon fiber bracket for magnetically suspended flywheel (MSFW)," *Acta Astronautica*, vol. 154, pp. 9–17, Jan. 2019.
[4] D. G. Christopher and R. Beach, "Flywheel technology development program for aerospace applications," *IEEE Aerosp. Electron. Syst. Mag.*, vol. 6, no. 13, pp. 9–14, Jun. 1997.
[5] H. Wang, J. Wu, Y. Li, and Y. Wu, "Design of reaction flywheel systems for small satellites," *Opt. Precis. Eng.*, vol. 22, no. 2, pp. 331–337, May 2014.
[6] S. D. Lee and S. Jung, "A compensation approach for nonlinear gimbal axis drift of a control moment gyroscope," *Mechatronics*, vol. 50, pp. 45–54, Apr. 2018.
[7] H. Li, X. Ning, and B. Han, "Composite decoupling control of gimbal servo system in double-gimbaled variable speed CMG via disturbance observer," *IEEE/ASME Trans. Mechatronics*, vol. 22, no. 1, pp. 312–320, Feb. 2017.
[8] X. Zhou, J. Sun, H. Li, M. Lu, and F. Zeng, "PMSM open-phase fault-tolerant control strategy based on four-leg inverter," *IEEE Trans. Power Electron.*, vol. 35, no. 3, pp. 2799–2808, Mar. 2020.
[9] H. Wang, Q. Han, and D. Zhou, "Output torque modeling of control moment gyros considering rolling element bearing induced disturbances," *Mech. Syst. Signal Process.*, vol. 115, pp. 188–212, Jan. 2019.
[10] W. MacKunis, F. Leve, P. M. Patre, N. Fitz-Coy, and W. E. Dixon, "Adaptive neural network-based satellite attitude control in the presence of CMG uncertainty," *Aerosp. Sci. Technol.*, vol. 54, pp. 218–228, Jul. 2016.
[11] G. Tyc, W. R. Whitehead, S. Pradhan, D. A. Staley, C. Ower, J. Cain, and M. Wiktowy, "Gyrowheel- an innovative new actuator/sensor for 3 axis spacecraft attitude control," in *Proc. 13th Annu. AIAA /USU Conf. Small Satellites*, Salt Lake City, Utah, USA, 1999, pp. 1–13.
[12] I. Walkty, J. Petersen, T. Doherty, and B. Whitehead, "SCISAT-1 ACE Mission C&DH Unit Development," in *Proc. 14th Annual AIAA /USU Conf. Small Satellites*, Salt Lake City, Utah, USA, USA, 2000, pp. 1–13.
[13] K. Sathyan, H. Y. Hsu, S. H. Lee, and K. Gopinath, "Long-term lubrication of momentum wheels used in spacecrafts—An overview," *Tribol. Int.*, vol. 43, nos. 1–2, pp. 259–267, Jan. 2010.

[14] L. Li, Y. Fan, and J. Yuan, "Application of magnetically suspended gimbaling flywheel in satellite attitude maneuver," *Chin. J. Mech. Eng.*, vol. 51, no. 16, pp. 206–212, Aug. 2015.

[15] C. Peng and Q. Zhou, "Direct vibration force suppression for magnetically suspended motor based on synchronous rotating frame transformation," *IEEE Access*, vol. 7, pp. 37639–37649, 2019.

[16] L. Qiang, W. Kun, R. Yuan, P. Peilan, M. Limei, and Y. Zhaojing, "Novel repeatable launch locking/unlocking device for magnetically suspended momentum flywheel," *Mechatronics*, vol. 54, pp. 16–25, Oct. 2018.

[17] C. Murakami, Y. Ohkami, O. Okamoto, A. Nakajima, M. Inoue, J. Tsuchiya, K. Yabu-uchi, S. Akishita, and T. Kida, "A new type of magnetic gimballed momentum wheel and its application to attitude control in space," *Acta Astronautica*, vol. 11, no. 9, pp. 613–619, Sep. 1984.

[18] J. Seddon and A. Pechev, "3-D wheel: A single actuator providing three-axis control of satellites," *J. Spacecraft Rockets*, vol. 49, no. 3, pp. 553–556, May 2012.

[19] Y. Horiuchi, M. Inoue, and N. Sato, "Development of magnetic bearing momentum wheel for ultra-precision spacecraft attitude control," in *Proc. 7th Int. Symp. Magnetic Bearings*, Zurich, Switzerland, 2000, pp. 525–530.

[20] W. Tong and F. Jiancheng, "A feedback linearization control for the nonlinear 5-DOF flywheel suspended by the permanent magnet biased hybrid magnetic bearings," *Acta Astronautica*, vol. 79, pp. 131–139, Oct. 2012.

[21] J. Tang, J. Sun, J. Fang, and G. Shuzhi Sam, "Low eddy loss axial hybrid magnetic bearing with gimballing control ability for momentum flywheel," *J. Magn. Magn. Mater.*, vol. 329, pp. 153–164, Mar. 2013.

[22] C. Peng, M. Zhu, K. Wang, Y. Ren, and Z. Deng, "A two-stage synchronous vibration control for magnetically suspended rotor system in the full speed range," *IEEE Trans. Ind. Electron.*, vol. 67, no. 1, pp. 480–489, Jan. 2020.

[23] Y. C. Xie, H. Sawada, T. Hashimoto, and K. Ninomiya, "Actively controlled magnetic bearing momentum wheel and its application to satellite attitude control," ISAS, Kanagawa, Japan, Tech. Rep. 680, Mar. 2001.

[24] M. Saito, K. Fukushima, N. Sato, K. Izawa, T. Hashimoto, and A. Nakajima, "Development of magnetic bearing wheel (MBW) with inclined magnetic poles (3rd report, low disturbance control based on disturbance Feedback)," *Trans. Jpn. Soc. Mech. Engineers Ser.*, vol. 72, no. 715, pp. 698–705, 2006.

[25] B. Gerlach, M. Ehinger, H. K. Raue, and R. Seiler, "Digital controller for a gimballing magnetic bearing reaction wheel," in *Proc. AIAA Guid., Navigat., Control Conf. Exhibit*, Aug. 2005, p. 6467.

[26] B. Liu, J. Fang, and G. Liu, "Design of a magnetically suspended Gyrowheel and analysis of key technologies," *Hangkong Xuebao/Acta Aeronautica et Astronautica Sinica*, vol. 32, no. 8, pp. 1478–1487, Aug. 2011.

[27] J. Li, K. Xiao, and K. Liu, "Mathematical model of a Vernier gimballing momentum wheel supported by magnetic bearings," in *Proc. 13th Int. Symp. Magn. Bearings*, Arlington, VA, USA, 2012, pp. 1–9.

[28] B. Xiang and J. Tang, "Suspension and titling of Vernier-gimballing magnetically suspended flywheel with conical magnetic bearing and lorentz magnetic bearing," *Mechatronics*, vol. 28, pp. 46–54, Jun. 2015.

[29] J. Tang, B. Xiang, and C. Wang, "Rotor's suspension for Vernier-gimballing magnetically suspended flywheel with conical magnetic bearing," *ISA Trans.*, vol. 58, pp. 509–519, Sep. 2015.

[30] Q. Liu, D. Hu, B. Wu, W. Meng, D. Liang, and X. Gao, "A magnetic suspension conical spherical gyro flywheel with external rotor," China Patent 2015 108 111 863, Aug. 4, 2017.

**HENG LI** was born in Shandong, China, in 1996. He received the B.S. degree in mechatronics engineering from the Harbin University of Science and Technology, Weihai, China, in 2017. He is currently pursuing the M.S. degree with the College of Mechanical Engineering, Beijing Institute of Petrochemical Technology.

His research interests include the design and active control of magnetic bearing.

**WEI WANG** received the B.S. degree in electronics engineering from the Jilin University of Technology, Changchun, China, in 1985, and the M.S. degree from the Department of Optical Instruments from the Changchun Institute of Optics, Fine Mechanics, and Physics, Chinese Academy of Sciences, Changchun, in 1992.

She is currently an Associate Professor with the Department of Mechanical Engineering, Beijing Institute of Petrochemical Technology. She has authored three books and more than 30 articles, and holds more than 15 inventions. Her research interests include the measurement and control technology of the magnetic bearing.
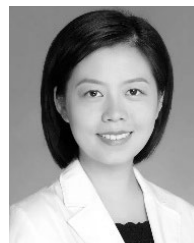
**CONG PENG** (Member, IEEE) received the B.S. degree in instrument science and technology from Southeast University, Nanjing, China, in 2010, and the Ph.D. degree in instrument science and technology from the Beijing University of Aeronautics and Astronautics, Beijing, China, in 2016.

She is currently a Professor with the College of Automation Engineering, Nanjing University of Aeronautics and Astronautics. Her research interests include active vibration control, vibration measurement, and computer vision.

**QIANG LIU** was born in Jiangxi, China, in 1983. He received the B.S. degree in mechanical engineering from the Beijing Institute of Petrochemical Technology, Beijing, China, in 2005, and the Ph.D. degree in instrument science and technology from the Beijing University of Aeronautics and Astronautics, Beijing, in 2013.

He is currently an Associate Professor with the Department of Mechanical Engineering, Beijing Institute of Petrochemical Technology. He has published more than 30 SCI/EI academic articles, one textbook, and one professional work, and authorized 47 national invention patents. His research interests include the inertial actuator, magnetic suspension support technology and application technology, Lorentz pod for remote sensing satellite, and military anti-rolling stable platform.
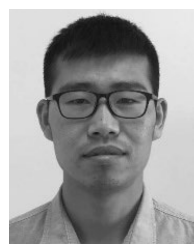
**ZENGYUAN YIN** was born in Henan, China, in 1993. He received the B.S. degree from the Shandong University of Technology, Zibo, China, in 2016, and the M.S. degree from Space Engineering University, Beijing, China, in 2018, where he is currently pursuing the Ph.D. degree.

His research interests mainly include the design and control of magnetic bearing and magnetic suspension inertial mechanism.

• • •